저작자표시-비영리-변경금지 2.0 대한민국

이용자는 아래의 조건을 따르는 경우에 한하여 자유롭게

- 이 저작물을 복제, 배포, 전송, 전시, 공연 및 방송할 수 있습니다.

다음과 같은 조건을 따라야 합니다:

저작자표시. 귀하는 원저작자를 표시하여야 합니다.

비영리. 귀하는 이 저작물을 영리 목적으로 이용할 수 없습니다.

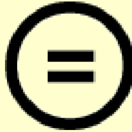

변경금지. 귀하는 이 저작물을 개작, 변형 또는 가공할 수 없습니다.

- 귀하는, 이 저작물의 재이용이나 배포의 경우, 이 저작물에 적용된 이용허락조건을 명확하게 나타내어야 합니다.
- 저작권자로부터 별도의 허가를 받으면 이러한 조건들은 적용되지 않습니다.

저작권법에 따른 이용자의 권리는 위의 내용에 의하여 영향을 받지 않습니다.

이것은 이용허락규약(Legal Code)을 이해하기 쉽게 요약한 것입니다.

Disclaimer

dCollection

공학석사 학위논문

2D Numerical modeling developments for inductively coupled plasma carburizing process

유도결합 플라즈마를 이용한 침탄공정의 2D 수치해석 모델개발에 대한 연구

February 2014

SEOKJIN KO

Department of material science and engineering

The Graduate school

SEOUL NATIONAL UNIVERSITY

Abstract

A 2D axis−symmetric numerical model using CFD−ACE was performed for plasma carburizing process. The particle conservation equation, drift−diffusion and energy conservation equation were used to calculate the density distribution of electrons and ions at various argon to methane gas ratios. It was found that the plasma, hydro−carbon ion densities and electron temperature increased with increasing the argon content in the carburizing chamber. During plasma carburizing, DC bias is applied to the substrate, thus the most important species for carburizing might be hydrocarbon ions. At low CH_4 fraction, the model predicted more amount of CH_x^+ ions are generated than $C_2H_y^+$ ions. The amount of free carbon, which diffuses into the substrate, during plasma carburization process was predicted by plasma modeling. The predictions of carbon concentration in the below substrate showed matching values to the experimental results.

Keyword: Inductively coupled plasma, ICP, carburizing, plasma simulation, CFD−ACE, plasma chemistry

Student Number: 2012−20575

Contents

I. Introduction 1

II. Research background 3

2.1. Inductively coupled plasma assisted plasma carburizing 3

2.2. Methane plasma chemistry 6

III. Experimental detail 8

3.1. Inductively coupled plasma carburizing 8

3.2. Plasma Model 11

3.2.1 Modeling assumption 11

3.2.2 Plasma heating model 12

3.2.3 Plasma chemistry set 14

IV. Result and discussion 25

4.1. Electron density distribution in internal inductively coupled plasma 25

4.2 Electron density compares with calculated data and experimental data 27

4.3 Ion mobility and diffusivity 27

4.4 Main species 29

4.5 X−ray diffraction Patterns of Carburized substrate 35

V. Conclusion 41

VI. Reference 42

국문초록 45

List of figures

Figure.2-1. Solenoid coil and induced magnetic field.

Figure.3-1. the schematic diagram of ICP diffusion process system.

Figure.4-1. plasma density and inductive heating distribution of time averaged plasma discharge.

Figure.4-2. Measured and calculated electron density.

Figure.4-3. Densities of main species calculated in CH_4/Ar plasma.
a) CH_x, hydrogen and Ar neutrals b) C_2H_y neutrals
c) CH_x and C_2H_y ions

Figure.4-4. Reaction paths of hydrocarbon ions.

Figure.4-5. Reaction paths of generating free carbon.

Figure.4-6. Temperatures of electrons calculated in CH_4/Ar plasma as a function of methane fraction.

Figure.4-7. Carbon atomic concentration depth profile by GD-OES.
a) X_{CH4} 25% b) X_{CH4} 50% c) X_{CH4} 75%

Figure.4-8. x-ray diffraction patterns of carburized AISI 316L

with X_{CH4} (25%, 50%, 75%).

Figure.4-9. Carbon atomic percent analyzed by GD-OES and XRD.

Figure.4-10. Comparison of deposition rates of C(s) predicted by plasma modeling and surface carbon atomic concentration measured by GDOES as a function of X_{CH4} fraction.

List of tables

Table. 3-1. Volume reaction of hydrogen

Table. 3-2. Reaction set for hydrocarbon and electron.

Table. 3-3. Reaction set for hydrocarbon ions-neutrals.

Table. 3-4. Reaction set for hydrocarbon neutral-neutrals.

Table. 3-5. Surface reaction sets for carburizing.

I. Introduction

Carburizing process has been used to enhance mechanical hardness. However, traditional thermal carburizing process needs to high temperature and very long process time.[2-9] Therefore, in recent days, plasma is widely used for carburizing process. By using plasma for carburizing process, there are lots of advantages compared with thermal carburizing. Most importantly, it can be done without high temperature so we can get rid of thermal damage to materials and reduce process time.

Various researchers had been studied the characteristic of methane plasma and its applications. K Bera (2001) developed 2-dimensional radio frequency inductively coupled plasma model to investigate effects of charged particle in the diamond like carbon deposition process.[32] I.B. Denysenko (2003) developed a spatially averaged discharge model to study PECVD (plasma enhanced chemical vapor deposition) process for aligned carbon nanostructures.[11] N. Fourches (1993) studied hydrogenated amorphous carbon layers deposited by r.f. discharge.[34] Takashi kimura (2012) studied CH_4/H_2 plasmas and experiments with a Langmuir probe and optical emission spectroscopy in inductively coupled RF plasma at 25, 50 and 100 mTorr for hydrogen fractions ranging from 0 to 80 %.[39]

Hong et al investigated the plasma carburizing process on proton exchange membrane fuel cell.[1] In his research, electric conductivity and corrosion resistance were improved when the carburizing process was conducted at low temperatures. Thus, by placing the substrate about 100 mm away from the coil, the operating temperature could be decreased while still having sufficient densities of ions and radials for the carburizing process. We developed 2D model to estimate the densities of ion and radials around the substrate area. The objectives of this research were investigating the effect of argon addition on plasma parameters in inductively coupled CH_4 plasma and understand surface reaction for carburizing process using the 2-dimensional model. Plasma volume reaction and surface reaction proposed in the previous research papers was used to understand plasma chemistry of methane and argon plasma

II. Research background

2.1 Inductively coupled plasma assisted plasma carburizing

Inductive discharge was first reported at the end of nineteen century. The principle is to induce an RF current in a plasma by driving an RF current in an antenna. The wave length of 13.56 RF is much longer than that of RF antenna; it can be solved by quasi−normal electromagnetic solutions. Fig.1 shows solenoid coil and induced magnetic field. From eq.2.1 and eq.2.2 magnetic field is induced by RF current proportional to n and RF current at antenna.

$H_z = nI$ (2.1)

$I = I_0 \sin \omega \mathrm{t}$ (2.2)

A magnetic flux (Φ) is represented eq.2.3. where μ_0 is permeability and r is radius of antenna.

$\Phi = \mu_0 \pi r^2 H_z$ (2.3)

Thus azimuthal electric field (E_θ)is proportional to antenna radius (r), number of turns (n), antenna current(I_0), driving RF frequency(ω).

$V_{ind} = 2\pi \mathrm{r} E_\theta = -\frac{\partial \Phi}{\partial t}$ (2.4)

$E_\theta(\mathrm{r,t}) = \frac{\mu_0 r}{2} \omega \mathrm{n} I_0 cos \omega \mathrm{t}$ (2.5)

The azimuthal electric field accelerates electrons and ions, which are ionized from neutral particles to maintain the plasma discharge. In the steady-state, the loss rate due to diffusion and the production rate due to ionization are balanced in the plasma. Maintaining a high plasma density is difficult because diffusion losses are increased and ionization production is lowered at low pressure. However, the ICP system can maintain a high plasma density because the collisions of electrons and ions continue to occur due to the induced electric field. Thus, the plasma density of ICP is 10~100 times higher than that of conventional plasma processes such as DC glow discharge or RF capacitive coupled plasma. The plasma density and ion energy to the substrate can also be independently controlled. The ICP discharge is the source of stable, reproducible, and highly uniform high-density plasmas and the plasma potential and electron temperature near the substrate appear to be low, which is favorable for the product yield, such as in etching and deposition processes. However, research into the use of the ICP diffusion processes on stainless steels has been limited to hardening of the surface of steels.

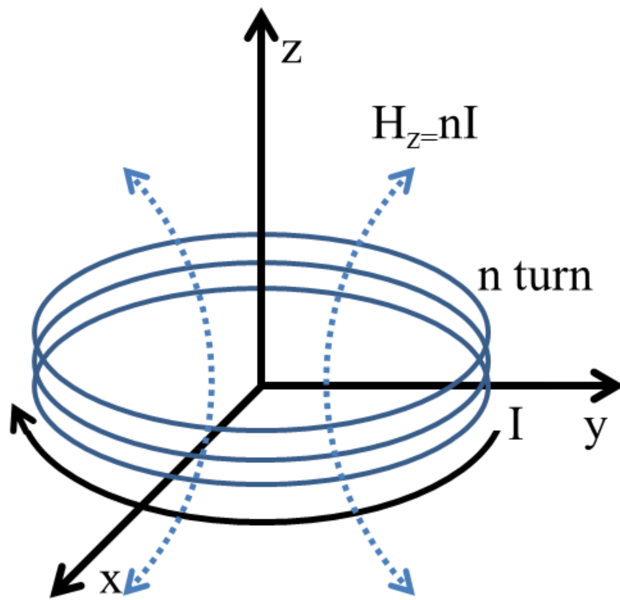

Figure.2-1 Solenoid coil and induced magnetic field

2.2. Methane plasma chemistry

Methane and methane/hydrogen plasmas have been used as reactant gases for the deposition of diamond−like carbon films and the conservation of oxidized iron archeological objects. In a methane discharge, the electron energy distribution function (EEDF) was found to be close to a Druyvesteynian distribution (Andres 1990) rather than a Maxwellian distribution.[31] A plasma model based on these measurements had predicted CH_3 as the most abundant neutral radical and CH_5^+ as the most abundant ionic species.

In this study, it was confirmed that ICP RF power, process pressure, process gas, DC bias applied to substrate is major knob of plasma carburizing process. ICP power and process pressure affects density of plasma and variety of radical. Controlling DC bias to substrate can be used to regulate ion energy. Thus, study the characteristics of the methane plasma is essential. In general, 6 angmuir probe, quadrupole mass spectrometer (QMS), optical emission spectroscopy (OES), laser induce fluorescence are used to analyze the characteristics of plasma, which are plasma density, types of ions, electron temperature and plasma potential. In case of Langmuir probe, it is almost impossible to investigate the types

of radical and ions. Besides, the area of measurements is not the surface area of Langmuir probe but the sheath region generated by Langmuir probe. Thus it should be considered to reduce a margin of error. Thus it is necessary to analysis information of sheath size. But analyzing for sheath size also has an uncertainty so it should be applied appropriately. In addition to that limitations, reactive chemical species are absorbed to probe that inserted to plasma and secondary electrons are generated by immersed probe. Thus it is restricted to analyze plasmas that contain highly reactive gas. OES makes measurements based on the information of wave that occurs when a species excited by electrons and ions is shifted to the ground state. Thus it is difficult to understand about heavy chemical species that is hardly excited to upper energy level. For quantitative measurement, reference data which contains intensity of certain wave is essential. QMS is mass analyzer used in mass spectroscopy. It has a quadrupole filter that classifies mass of chemical species. So it can investigate radical and neutral molecules relatively accessible and accurate. It is difficult to obtain informations of substrate region. Thus developing methane plasma chemistry and estimate properties of plasma adjacent of substrate can provide valuable information.

III. Experimental detail

3.1 Inductively coupled plasma carburizing

Device configuration of plasma carburizing reactor used in this study is shown in fig.3-1 The discharge reactor had a cylindrical shape with an inner radius is 67mm and a coil was inserted in the reactor. The quartz chamber is used and coil was made of stainless steel. A hot wall heater was mounted outside of the quartz chamber to regulate the temperature of the substrate. An RF power of 13.56MHz was applied to the two turn ICP antenna through pi type RF matcher and DC bias power was applied to the substrate. A substrate was floated from ground potential of discharge reactor, so substrate potential could be pulled down to negative potential. The flow rates of CH_4 and Ar gas were controlled by mass flow controllers separately, and total amount of mixed gas was 20 sccm. Ferrite core ring was installed to input terminal of mass flow rate controller in order to remove RF noise. A cylindrical probe was installed at the axial center of the reactor to measure ion saturation currents. Commercial AISI 316L austenitic stainless steel with a chemical compositions of 0.03wt% C, 2wt% Mo, 12wt% Ni, 18wt%Cr, and balance Fe was

used in this study. Samples with thickness of 0.3 mm and 0.2mm were cut into a size of 40 x 50 mm^2 pieces and were then cleaned ultrasonically with acetone and ethanol each during 15 minutes in that order.

Before process, the system was evacuated to 1 x 10^{-4} Pa and the sample was plasma-etched with hydrogen and argon to remove the surface native oxide.

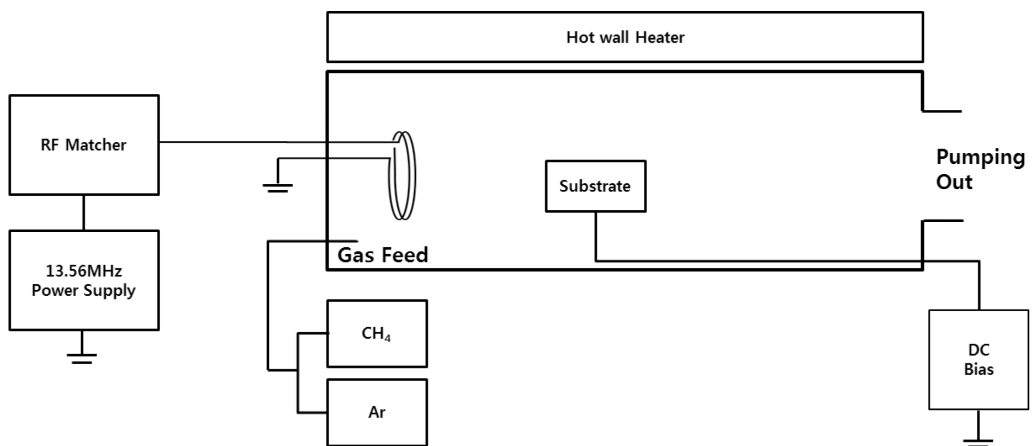

Figure.3-1 the schematic diagram of ICP diffusion process system

3.2 Plasma Model

3.2.1 Modeling assumption

In our study, the plasma carburizing model was developed using CFD−ACE GUI, CFD−ACE GEOM. The particle conservation equation eq.3.1 drift−diffusion approximation equ.3.2 and energy conservation equation eq.3.3 were used to calculate transport of electrons.

$$\frac{\partial n_e}{\partial t} + \nabla \cdot \overrightarrow{\Gamma_e} = S \quad (3.1)$$

$$\overrightarrow{\Gamma_e} = \mu_e n_e \nabla\varphi - D_e \nabla n_e \quad (3.2)$$

$$\frac{3}{2}\frac{\partial}{\partial t}(n_e T_e) + \nabla\left(\frac{5}{2} T_e \overrightarrow{\Gamma_e} - \chi \nabla T_e\right) = P - n_e \sum_r n_r k_r \varepsilon_r \quad (3.3)$$

Γ_e is the electron density flux, and S is the source of electrons produced or consumed in chemical reaction, n_e is the electron density, D_e is the diffusion coefficient, φ is the electrostatic potential, T_e is the electron temperature. The electron energy distribution is assumed as Maxwellian.

Ion mobility was calculated using Einstein’s relation equ.3.4.

$$\mu_i = \frac{D_i}{T_i} \text{ (assumed } T_i = T_{gas}\text{)} \quad (3.4)$$

Sheath size of inductively coupled plasma is much smaller than capacitively coupled plasma, the physics occurring in the sheath is minor inportant when inductively coupled plasma operates in

H−mode discharge. And electric potential fluctuation in plasma volume is weak so we assumed that a treatment of the bulk plasma as quasi−neutral. It would eleminate the need to solve Poisson's equation.(equ.3.5, equ.3.6) Using quasi−neutrality assumtion we could reduce lots of time so we could calculate lots of plasma chemistry reaction sets. Associated with quasi−neutral assumtion, collisionless sheath models are applied to calculate Ion Energy Distribution Function (IEDF) at a biased electrode.

$n_e = \sum q_i n_i$ (3.5)

$E = -\frac{D_e \nabla n_e}{\mu_e n_e} = -T_e \nabla \ln(n_e)$ (3.6)

3.2.2 Plasma heating model

Plasma carburizing process was assumed it operated in high density discharge mode so inductive heating was dominant compared with capacitive heating. The inductive heating equ.3.7 is function of complex electric conductivity ($\tilde{\sigma}$), angular frequency of RF source(ω), vector magnetic potential ($\tilde{A}$) and complex electric conductivity is equ.3.8.

$P_{ind} = \frac{1}{2} Re(\tilde{\sigma}) \omega^2 |\tilde{A}|^2$ (3.7)

$\tilde{\sigma} = \frac{\varepsilon_0 \omega_{ep}}{\nu_m + \omega i}$ (3.8)

$\varepsilon_0, \omega_{ep}, \nu_m$ Denotes permittivity of free space, electron plasma frequency, electron collision frequency.

3.2.3 Plasma chemistry sets for carburizing

Table. 3-1. Volume reaction of hydrogen

No	Reaction	Rate constant (m^3/s)	Ref.
1	$H_2 + e \rightarrow H_2 + e$	collision cross section (momentum transfer)	46
2	$H_2 + e \rightarrow H_2 + e$	collision cross section (rotational excitation J=0→2)	46
3	$H_2 + e \rightarrow H_2 + e$	collision cross section (rotational excitation J=1→3)	46
4	$H_2 + e \rightarrow H_2 + e$	collision cross section (vibrational excitation 0.516)	46
5	$H_2 + e \rightarrow H_2 + e$	collision cross section (vibrational excitation 1.0)	46
6	$H_2 + e \rightarrow H_2 + e$	collision cross section (vibrational excitation 1.5)	46
7	$H_2 + e \rightarrow H_2 + e$	collision cross section (electronic excitation 8.9 B[3]sigma)	46
8	$H_2 + e \rightarrow H_2 + e$	collision cross section (electronic excitation 11.3 B[1]sigma)	46
9	$H_2 + e \rightarrow H_2 + e$	collision cross section (electronic excitation 11.75 C[2]pi)	46
10	$H_2 + e \rightarrow H_2 + e$	collision cross section (electronic excitation 11.8 A[3]sigma)	46
11	$H_2 + e \rightarrow H_2 + e$	collision cross section (electronic excitation 12.4 C[1]pi)	46
12	$H_2 + e \rightarrow H_2 + e$	collision cross section (electronic excitation 14.0 D[3]pi)	46

13	$H_2 + e \rightarrow H_2 + e$	collision cross section (electronic excitation 15.2 Rydberg)	46
14	$H_2 + e \rightarrow 2H + e$	collision cross section (dissociative excitation 15.0 H(n=2))	46
15	$H_2 + e \rightarrow 2H + e$	collision cross section (dissociative excitation 16.6 H(n=3))	46
16	$H_2 + e \rightarrow H_2^+ + 2e$	Ionization	46
17	$H + e \rightarrow H^+ + 2e$	Ionization	46
18	$H_2^+ + e \rightarrow H^+ + H + e$	$1.45\times10^{-13}\exp(-1.97/T_e)$	46
19	$H_3^+ + e \rightarrow H_2 + H$	$1.55\times10^{-13}\exp(300/T_g)$	46
20	$H_2 + H_2^+ \rightarrow H_3^+ + H$	2.10×10^{-15}	46

Table. 3-2. Reaction set for hydrocarbon and electron

No	Reaction	Rate constant (m^3/s)	Ref.
21	$CH_4 + e \rightarrow CH_4^+ + 2e$	$3.17\times10^{-14}exp(-14.6/T_e)$	37
22	$CH_4 + e \rightarrow CH_3^+ + H + 2e$	$2.67\times10^{-14}exp(-16.4/T_e)$	37
23	$CH_3 + e \rightarrow CH_3^+ + 2e$	$2.35\times10^{-14}exp(-14.7/T_e)$	38
24	$CH_3 + e \rightarrow CH_2^+ + H + 2e$	$1.62\times10^{-14}exp(-17.0/T_e)$	38
25	$CH_2 + e \rightarrow CH_2^+ + 2e$	$2.35\times10^{-14}exp(-14.7/T_e)$	38
26	$CH_2 + e \rightarrow CH^+ + H + 2e$	$1.21\times10^{-14}exp(-20.5/T_e)$	38
27	$CH + e \rightarrow CH^+ + 2e$	$2.35\times10^{-14}exp(-14.7/T_e)$	38
28	$CH + e \rightarrow C^+ + H + 2e$	$5.57\times10^{-15}exp(-19.6/T_e)$	38
29	$C + e \rightarrow C^+ + 2e$	$4\times10^{-14}exp(-12.6/T_e)$	38
30	$C_2H_6 + e \rightarrow C_2H_6^+ + 2e$	$1.68\times10^{-14}exp(-12.2/T_e)$	38
31	$C_2H_6 + e \rightarrow C_2H_5^+ + H + 2e$	$1.21\times10^{-14}exp(-14.1/T_e)$	38
32	$C_2H_6 + e \rightarrow C_2H_4^+ + H_2 + 2e$	$6.11\times10^{-14}exp(-14.1/T_e)$	38
33	$C_2H_5 + e \rightarrow C_2H_5^+ + 2e$	$1.53\times10^{-14}exp(-12.2/T_e)$	38

34	$C_2H_5 + e \rightarrow C_2H_4^+ + H + 2e$	$1.10\times10^{-14}exp(-14.1/T_e)$	38
35	$C_2H_5 + e \rightarrow C_2H_3^+ + H_2 + 2e$	$5.55\times10^{-14}exp(-14.1/T_e)$	38
36	$C_2H_4 + e \rightarrow C_2H_3^+ + H + 2e$	$1.01\times10^{-14}exp(-14.1/T_e)$	38
37	$C_2H_4 + e \rightarrow C_2H_2^+ + H_2 + 2e$	$5.12\times10^{-14}exp(-14.1/T_e)$	38
38	$C_2H_3 + e \rightarrow C_2H_3^+ + 2e$	$1.36\times10^{-14}exp(-12.2/T_e)$	38
39	$C_2H_3 + e \rightarrow C_2H_2^+ + H + 2e$	$9.82\times10^{-15}exp(-14.1/T_e)$	38
40	$C_2H_3 + e \rightarrow C_2H^+ + H_2 + 2e$	$4.97\times10^{-14}exp(-14.1/T_e)$	38
30	$C_2H_2 + e \rightarrow C_2H_2^+ + 2e$	$3.73\times10^{-14}exp(-12.2/T_e)$	37
31	$C_2H_2 + e \rightarrow C_2H^+ + H + 2e$	$2.69\times10^{-14}exp(-14.1/T_e)$	37
32	$C_2H + e \rightarrow C_2H^+ + 2e$	$3.53\times10^{-14}exp(-12.2/T_e)$	38
33	$C_2H + e \rightarrow C^+ + C + H + 2e$	$2.77\times10^{-14}exp(-14.1/T_e)$	38
34	$CH_4 + e \rightarrow CH_3 + H + e$	$1.65\times10^{-14}exp(-9.71/T_e)$	37
35	$CH_4 + e \rightarrow CH_2 + 2H + e$	$1.85\times10^{-14}exp(-10.7/T_e)$	37
36	$CH_4 + e \rightarrow CH + 3H + e$	$2.07\times10^{-14}exp(-11.7/T_e)$	37
37	$CH_4 + e \rightarrow C + 4H + e$	$2.29\times10^{-14}exp(-12.6/T_e)$	37
38	$CH_3 + e \rightarrow CH_2 + H + e$	$4.10\times10^{-14}exp(-11.3/T_e)$	38

39	$CH_3 + e \rightarrow CH + 2H + e$	$1.69\times10^{-14}exp(-10.3/T_e)$	38
40	$CH_2 + e \rightarrow CH + H + e$	$2.37\times10^{-14}exp(-11.3/T_e)$	38
41	$CH_2 + e \rightarrow C + 2H + e$	$9.77\times10^{-15}exp(-10.3/T_e)$	38
42	$CH + e \rightarrow C + H + e$	$1.94\times10^{-14}exp(-11.3/T_e)$	38
43	$C_2H_6 + e \rightarrow C_2H_5 + H + e$	$1.08\times10^{-13}exp(-11.3/T_e)$	38
44	$C_2H_6 + e \rightarrow C_2H_4 + 2H + e$	$4.45\times10^{-14}exp(-10.3/T_e)$	38
45	$C_2H_5 + e \rightarrow C_2H_4 + H + e$	$1.05\times10^{-13}exp(-11.3/T_e)$	38
46	$C_2H_5 + e \rightarrow C_2H_3 + 2H + e$	$4.37\times10^{-14}exp(-10.3/T_e)$	38
47	$C_2H_4 + e \rightarrow C_2H_3 + H + e$	$1.08\times10^{-13}exp(-11.3/T_e)$	38
48	$C_2H_4 + e \rightarrow C_2H_2 + 2H + e$	$4.13\times10^{-14}exp(-10.3/T_e)$	38
49	$C_2H_3 + e \rightarrow C_2H_2 + H + e$	$9.17\times10^{-14}exp(-11.3/T_e)$	38
50	$C_2H_3 + e \rightarrow C_2H + 2H + e$	$3.78\times10^{-14}exp(-10.3/T_e)$	38
51	$C_2H_2 + e \rightarrow C_2H + H + e$	$1.31\times10^{-13}exp(-11.3/T_e)$	37
52	$C_2H + e \rightarrow C_2 + H + e$	$1.16\times10^{-13}exp(-11.3/T_e)$	38

Table. 3−3. Reaction set for hydrocarbon ions−neutrals

No	Reaction	Rate constant (m^3/s)	Ref.
53	$CH_5^+ + C_2H_6 \rightarrow C_2H_5^+ + H_2 + CH_4$	5.0×10^{-16}	11
54	$CH_4^+ + CH_4 \rightarrow CH_5^+ + CH_3$	1.5×10^{-15}	11
55	$CH_4^+ + H_2 \rightarrow CH_5^+ + H$	3.3×10^{-17}	11
56	$CH_3^+ + CH_4 \rightarrow CH_4^+ + CH_3$	1.36×10^{-16}	11
57	$CH_3^+ + CH_4 \rightarrow C_2H_5^+ + H_2$	1.2×10^{-15}	11
58	$H_3^+ + C_2H_6 \rightarrow C_2H_5^+ + 2H_2$	2.0×10^{-15}	11
59	$H_3^+ + CH_4 \rightarrow CH_5^+ + H_2$	1.6×10^{-15}	11,25
60	$H_3^+ + C_2H_4 \rightarrow C_2H_5^+ + H_2$	1.9×10^{-15}	11,25
61	$H_3^+ + C_2H_2 \rightarrow C_2H_3^+ + CH_3$	1.94×10^{-15}	11,25
62	$C^+ + CH_4 \rightarrow C_2H_2^+ + H_2$	4.0×10^{-16}	25
63	$C^+ + CH_4 \rightarrow C_2H_3^+ + H$	8.0×10^{-16}	25
64	$CH^+ + CH_4 \rightarrow C_2H_3^+ + H_2$	1.09×10^{-15}	25
65	$CH_2^+ + CH_4 \rightarrow C_2H_4^+ + H_2$	8.4×10^{-16}	25

66	$CH_2^+ + CH_4 \rightarrow C_2H_2^+ + 2H_2$	3.97×10^{-16}	25
67	$CH_2^+ + H_2 \rightarrow CH_3^+ + H$	1.6×10^{-15}	25
68	$C_2H_2^+ + CH_4 \rightarrow C_2H_3^+ + CH_3$	4.1×10^{-15}	11,25
69	$C_2H_2^+ + CH_4 \rightarrow C_2H_5^+ + H$	1.44×10^{-15}	25
70	$C_2H_3^+ + CH_4 \rightarrow C_3H_5^+ + H_2$	1.7×10^{-16}	25
71	$C_2H_3^+ + C_2H_4 \rightarrow C_2H_5^+ + C_2H_2$	2.3×10^{-16}	25

Table. 3-4. Reaction set for hydrocarbon neutral-neutrals

No	Reaction	Rate constant (m^3/s)	Ref.
72	$H + CH_4 \rightarrow CH_3 + H_2$	$2.2\times10^{-26}T_g^{3}exp(-4046/T_g)$	11
73	$H + CH_3 \rightarrow CH_2 + H_2$	$1.0\times10^{-16}exp(-7600/T_g)$	11,25
74	$H + CH_3 \rightarrow CH_4$	7.0×10^{-18}	21
75	$H + CH_2 \rightarrow CH + H_2$	$1.0\times10^{-17}exp(-900/T_g)$	11
76	$H + C_2H_6 \rightarrow C_2H_5 + H_2$	$2.4\times10^{-21}T_g^{1.5}exp(-3730/T_g)$	11
77	$H + C_2H_5 \rightarrow 2C_2H_3$	6.0×10^{-17}	11
78	$H + C_2H_5 \rightarrow C_2H_4 + H_2$	5.0×10^{-17}	11
79	$H + C_2H_4 \rightarrow C_2H_3 + H_2$	$9.0\times10^{-16}exp(-7500/T_g)$	11,25
80	$H + C_2H_3 \rightarrow C_2H_2 + H_2$	1.66×10^{-17}	25
81	$H + C_2H_2 \rightarrow C_2H + H_2$	$1.0\times10^{-16}exp(-14000/T_g)$	11
82	$CH_4 + C \rightarrow C_2H_2 + H_2$	1.0×10^{-17}	25
83	$CH_3 + CH_3 \rightarrow C_2H_6$	6.0×10^{-17}	11
84	$CH_3 + CH_3 \rightarrow C_2H_5 + H$	$5.0\times10^{-17}exp(-6800/T_g)$	11

85	$CH_3 + CH_3 \rightarrow C_2H_4 + H_2$	$1.7\times10^{-14}\exp(-16000/T_g)$	11
86	$CH_3 + CH_2 \rightarrow C_2H_4 + H$	7.0×10^{-17}	11
87	$CH_3 + CH \rightarrow C_2H_3 + H$	5.0×10^{-17}	11
88	$CH_2 + CH_2 \rightarrow C_2H_4$	1.7×10^{-18}	11
89	$CH_2 + CH_2 \rightarrow C_2H_2 + H_2$	$2.0\times10^{-16}\exp(-400/T_g)$	11
90	$CH + CH_4 \rightarrow C_2H_4 + H$	1.0×10^{-16}	11
91	$CH + CH_2 \rightarrow C_2H_2 + H$	6.6×10^{-17}	11
92	$CH + CH \rightarrow C_2H_2$	2.0×10^{-16}	11
93	$CH + H_2 \rightarrow CH_2 + H$	3.03×10^{-17}	14
94	$CH + H \rightarrow C + H_2$	4.98×10^{-17}	14
95	$C_2H_5 + CH_3 \rightarrow C_3H_8$	4.2×10^{-18}	11
96	$C_2 + H_2 \rightarrow C_2H + H$	1.4×10^{-18}	14
97	$Ar^+ + H_2 \rightarrow Ar + H_2^+$	2.7×10^{-16}	13
98	$Ar^+ + CH_4 \rightarrow Ar^+ + H + CH_3^+$	1.05×10^{-15}	13
99	$Ar^+ + H_2 \rightarrow ArH^+ + H$	1.6×10^{-15}	13

Table. 3-5. Surface reaction sets for carburizing

No	Surface reaction	Parameters	Ref.
1	$CH_{3(plasma)} \rightarrow CH_{3(ads)}$	$S_{0,CH3} = 1$	30,32
2	$CH_{2(plasma)} \rightarrow CH_{2(ads)}$	$S_{0,CH2} = 1$	30,32
3	$H_{(plasma)} \rightarrow H_{(ads)}$	$S_{0,H} = 1$	30,32
4	$CH_{3(ads)} \rightarrow CH_{3(des)}$	$E_{des} = 0.65eV, \tau_0 = 10^{-12}s, \nu_0 = 1.3\times10^{19}m^{-2}$	30,32
5	$CH2_{(ads)} \rightarrow CH_{2(des)}$	$E_{des} = 0.65eV, \tau_0 = 10^{-12}s, \nu_0 = 1.3\times10^{19}m^{-2}$	30,32
6	$H_{(ads)} \rightarrow H_{(des)}$	$E_{des} = 0.65eV, \tau_0 = 10^{-12}s, \nu_0 = 1.3\times10^{19}m^{-2}$	30,32
7	$CH_{3(ads)} + H_{(plasma)} \rightarrow CH_{4(plasma)}$	$\sigma_{ads} = 6.8\times10^{-20}m^2$	30,32
8	$CH_{2(ads)} + H_{(plasma)} \rightarrow CH_{3(plasma)}$	$\sigma_{ads} = 6.8\times10^{-20}m^2$	30,32
9	$H_{(ads)} + H_{(plasma)} \rightarrow H_{2(plasma)}$	$\sigma_{ads} = 6.8\times10^{-20}m^2$	30,32
10	$CH_5^+ \rightarrow C_{(s)} + 3H_{(s)} + H_{2(plasma)}$	$S_{0,CH5+} = 1$	39
11	$CH_4^+ \rightarrow C_{(s)} + 2H_{(s)} + H_{2(plasma)}$	$S_{0,CH4+} = 1$	39
12	$CH_3^+ \rightarrow C_{(s)} + H_{(s)} + H_{2(plasma)}$	$S_{0,CH3+} = 1$	39
13	$CH_2^+ \rightarrow C_{(s)} + H_{2(plasma)}$	$S_{0,CH2+} = 1$	39

14	$C_2H_5^+ \rightarrow$ $2C_{(s)} + 3H_{(s)} + H_{2(plasma)}$	$S_{0,C2H5+} = 1$	39
15	$C_2H_3^+ \rightarrow$ $2C_{(s)} + H_{(s)} + H_{2(plasma)}$	$S_{0,C2H3+} = 1$	39
16	$c_bH_{(s)} \rightarrow$ $0.25H_{2(plasma)} + (c_b - y_{ch})H_{(s)}$	$y_{ch} = 0.5$	30,32
17	$C_{(s)} + c_bH_{(s)} + (4 - c_b)H_{(plasma)} \rightarrow$ $CH_{4(plasma}$	$\sigma_{et} = 1.0\times10^{-21}m^2$	39
18	$Ar^+ + CH_2(s) \rightarrow$ $C_{(s)} + H_2 + Ar^+{}_{(plasma)}$	$Y_d=2.49\times10^{-2}+3.29\times10^{-2}\varepsilon_i$	30,32
19	$Ar^+ + CH_3(s) \rightarrow$ $C_{(s)} + H_2 + H_{(s)} + Ar^+{}_{(plasma)}$	$Y_d=2.49\times10^{-2}+3.29\times10^{-2}\varepsilon_i$	30,32
20	$Ar^+ + H(s) \rightarrow H + Ar^+{}_{(plasma)}$	$Y_d=2.49\times10^{-2}+3.29\times10^{-2}\varepsilon_i$	30,32
21	$CH_n^+ + CH_2(s) \rightarrow C_{(s)} + H_{(s)} +$ $H_{(plasma)} + CH_n^+$	$Y_d=2.49\times10^{-2}+3.29\times10^{-2}\varepsilon_i$	30,32
22	$CH_n^+ + CH_3(s) \rightarrow C_{(s)} + 2H_{(s)} +$ $H_{(plasma)} + CH_n^+$	$Y_d=2.49\times10^{-2}+3.29\times10^{-2}\varepsilon_i$	30,32

IV. Result and discussion

4.1. Electron density distribution in internal inductively coupled plasma

In this study, axial time distribution of plasma characteristics i.e. electron, neutral/radical/ion number density was calculated and measured, while gas pressure was maintained at 40 mTorr with changing the flow rates of CH_4 and Ar. Figure.4-1 shows that electron number density of inductively coupled plasma and region of inductive heating occurs. Maximum plasma density and electron temperature were measured in the center of radial axis between the internal inductively coupled plasma antennas. Strong inductive heating is generated, according to the azimuthal electric field is induced around the internal inductively coupled plasma antenna. In general, low pressure plasma discharge presents plasma skin depth of several tens of millimeters in the azimuthal electric field. In order to accurate calculation of the absorption power density in the skin depth, separate the distance between the cells in the skin depth region must be small than 1mm. Most reactions occurred in the region where density and temperature of electrons were maximized.

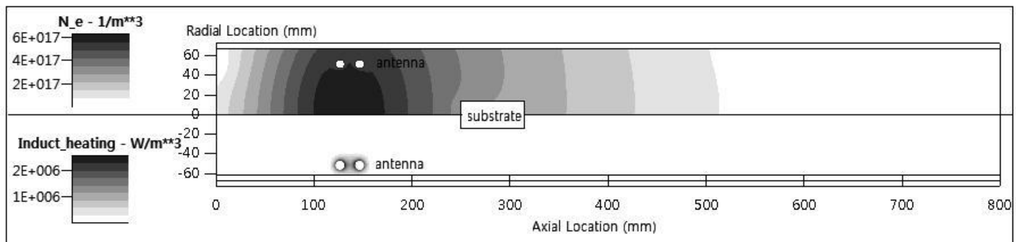

Figure.4−1 plasma density and inductive heating distribution of time averaged plasma discharge

(Pressure = 40 mTorr, electron absorbed power = 240 W, CH_4 = 5 sccm, Ar = 15 sccm)

4.2. Electron density compares with calculated data and experimental data

Fig.4-2 shows a comparison of the electron density between experimentally measured and calculated results, obtaining reasonably good agreement. However the measured plasma density decreases more rapidly than the simulated data, as far from the ICP antenna. In our plasma model, we didn' t include energy loss which generate from excitation of ground state methane neutrals. So, it can be a possible cause for the little dissimilarity between the calculated and measured electron densities in Fig.4-2.

4.3. Ion mobility and diffusivity

Most of ions generated from maximum plasma density region are diffused to substrate region. So, knowledge of ion mobility and diffusivity can be key parameters to validate the 2D diffusion simulation. Trindade et al reported that mobility of methane ion was 6.8 $m^2V^{-1}s^{-1}$ at 5.32 Pa.[10] In our model, calculated methane ion mobility was 7.0 $m^2V^{-1}s^{-1}$obtaining reasonably accurate values. Therefore, it is possibly consider methane ion densities at substrate were practical values.

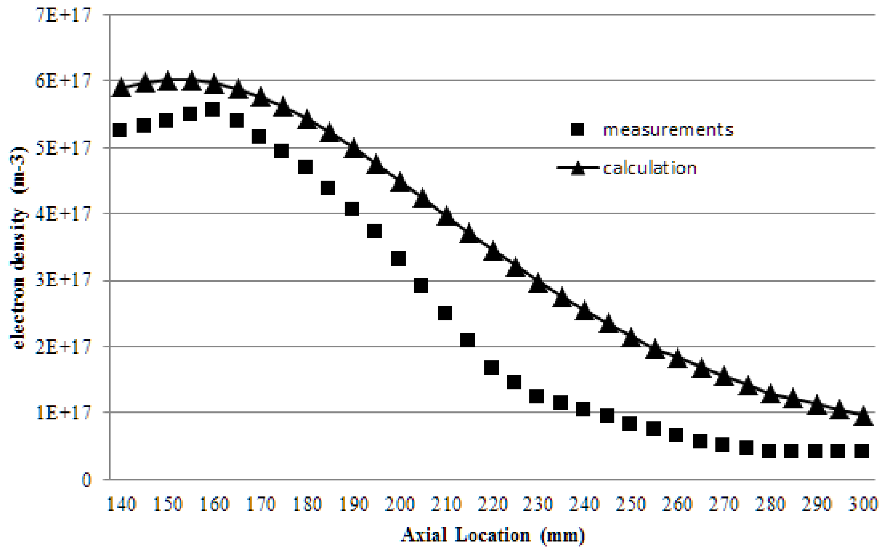

Figure.4-2 Measured and calculated electron density.

(Pressure = 40 mTorr, electron absorbed power = 240 W, CH_4 = 5sccm, Ar = 15 sccm)

*electron density was measured from ion saturation current and assumed that electron temperature is 2ev

4.4. Main species

Densities of main species are shown in fig. 4−3. The number density of CH_4 and its fragments such as CH_3 and CH_2 increases with CH_4 fraction. C_2H_y molecules are generated by collisions between CH_x molecules, so its number densities are proportional to CH_x and increase with CH_4 fraction. However, the number density of CH_x^+ ions such as CH_3^+, CH_4^+, and CH_5^+ decreases as CH_4 fraction increases while $C_2H_y^+$ ions such as $C_2H_4^+$ and $C_2H_6^+$ show opposite trend.

During plasma carburizing, DC bias is applied to the substrate, thus the most important species for carburizing might be hydrocarbon ions. It is essential to consider the reaction paths generating hydrocarbon ions.

First, CH_x^+ ions are produced by electron impact (dissociative) ionization of CH_x molecules, or by collision with Ar^+ ion with CH_x molecules. It is notable that CH_5^+ ion comes from the reaction between CH_4 and CH_4^+ shown in Eq. 54) of reaction set, and the density of CH_5^+ ions can be understood by following the reaction paths of CH_4^+ ion. The density of CH_x^+ ions is naturally proportional to that of CH_4, the source molecule. However, calculated densities do not follow the trend due to the electron temperature. There will be more

hydrocarbon molecules with CH_4 fraction. From the energy balance equation, the electron temperature (LHS of eq.3) decreases as energy consumed for chemical reactions (2nd term of RHS of eq.3) increases. It is shown in fig.4-5. The reactions for generating CH_x^+ ions have threshold energy of T_e, and the rate will be exponentially reduced as T_e decreases.

Second, the number density of $C_2H_y^+$ ions rises with CH_4 fraction. It can be resulted from two main sources; one kind is energy-independent CH_x^+ CH_x^+ reactions and the other T_e-dependent electron impact ionizations. Although CH_x^+ ions are less generated at higher CH_4 fractions, the densities of CH_x molecules are higher at those fractions. So, the associative reactions between CH_x and CH_x^+ molecules could produce more $C_2H_y^+$ ions. The density of C_2H_y neutral molecules and the electron temperature have opposite effect on the density of $C_2H_y^+$ ions. The C_2H_y molecules are more produced as CH_4 fraction increases. Finally, CH_x^+ ions are more generated than $C_2H_y^+$ ions at low CH_4 fraction.

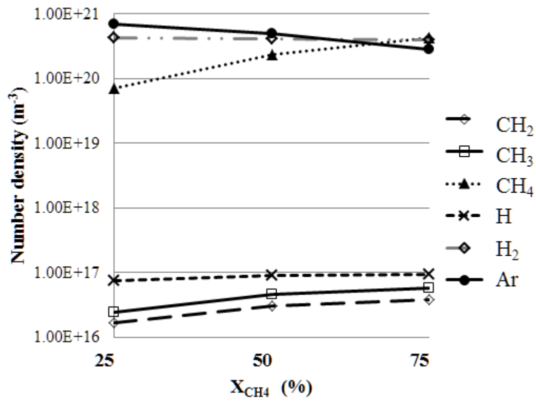

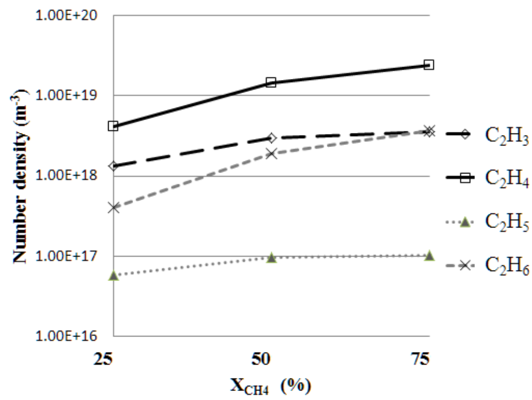

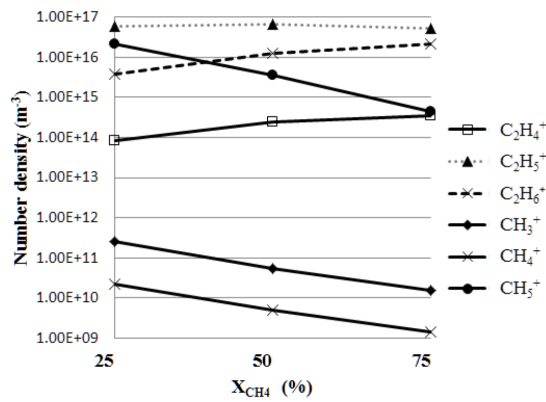

Figure.4-3 Densities of main species calculated in CH_4/Ar plasma

a) CH_x, hydrogen, and Ar neutrals, b) C_2H_y neutrals,

c) CH_x and C_2H_y ions

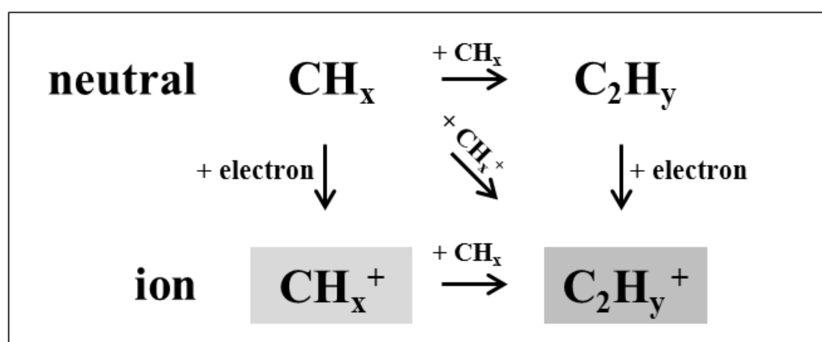

Figure.4－4 Reaction paths of hydrocarbon ions.

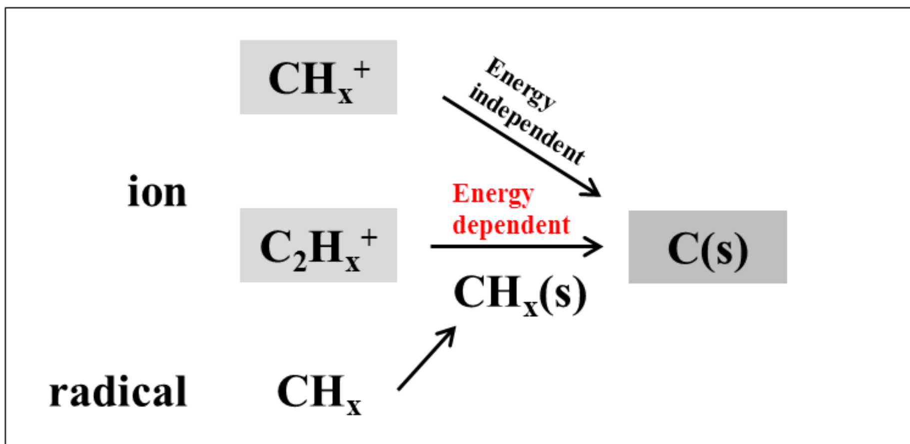

Figure.4-5 Reaction paths of generating free carbon.

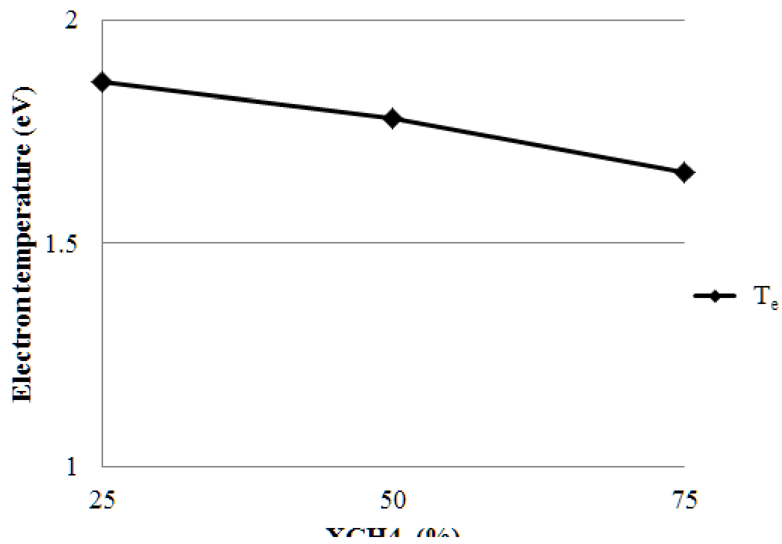

Figure.4-6 Temperatures of electrons calculated in CH_4/Ar plasma as a function of methane fraction. (Pressure=5.32Pa, electron absorbed power=240W)

4.5 X-ray diffraction Patterns of Carburized substrate

Fig. 7 represents XRD patterns of the carburized samples with various X_{CH4}. It can be seen that γ (111), γ (200), and γ (220) peak of austenite stainless peaks were shifted toward lower angle by carburizing process. The carbon atoms are diffused to stainless steel, and it increased the FCC lattice size of the stainless steel. The phase formed by carbon dissolution is expressed as γ_c. As the argon gas ratio increased, shift of γ_c peak is gradually increased. The approximate carbon content of the γ_c phase was calculated from XRD peak shifts using Picard' s equation. The values of expanded austenite lattice parameter was used average of (111) and (200) planes.

$a_{\gamma c} = a_{\gamma} + AC_c$

$a_{\gamma c}$: expanded austenite lattice parameter

a_{γ} : received austenite lattice parameter

A : Vegard's constant (0.0078Å)

C_c : atomic carbon concentration in lattice

Fig.8 is the result of atomic concentration percent of carbon existing on surface and inside of substrate when changing the ratio of methane and argon during carburizing process. As it was mentioned above, the carbon concentration in the substrate

was predicted by estimating the shift in the x-ray diffraction patterns of the carburized AISI 316L with respect to bare AISI 316L using the Picard equation. Also the atomic concentration percent of carbon in the surface and the inside of substrate was confirmed by analyzing the carburized sample using GDOES. As the gas flows of methane decreased and argon increased, the amount of carbon increased on the surface and inside of substrate. Therefore, carbon concentrations on the surface and the inside of substrate are proportional to each other, it confirm that the carburization process is a diffusion controlled process. Our plasma modeling was work to predict the amount of free carbon, which diffuses into the substrate, during plasma carburization process. The amounts of ions and radicals produced in the plasma volume and their impinge rates on the surface were estimated in the plasma carburizing model. The test results and the model estimations were compared. As shown in Fig.8, surface carbon atomic concentration measured by GDOES depend on X_{CH4}.The model results also show the dependence of deposition rates of C(s) on X_{CH4}.

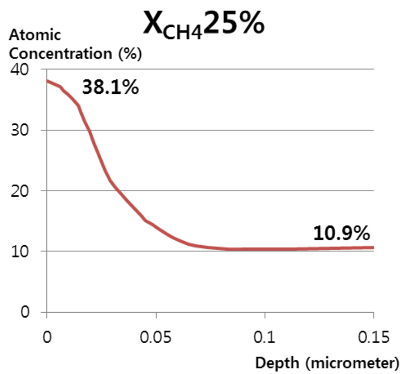

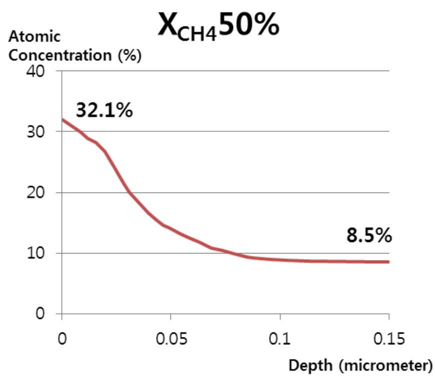

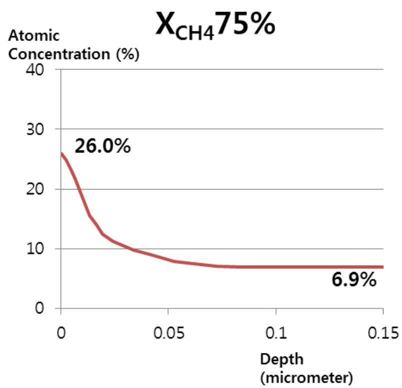

Figure.4-7 Carbon atomic concentration depth profile by GD-OES
a) X_{CH4} 25%, b) X_{CH4} 50%, c) X_{CH4} 75%

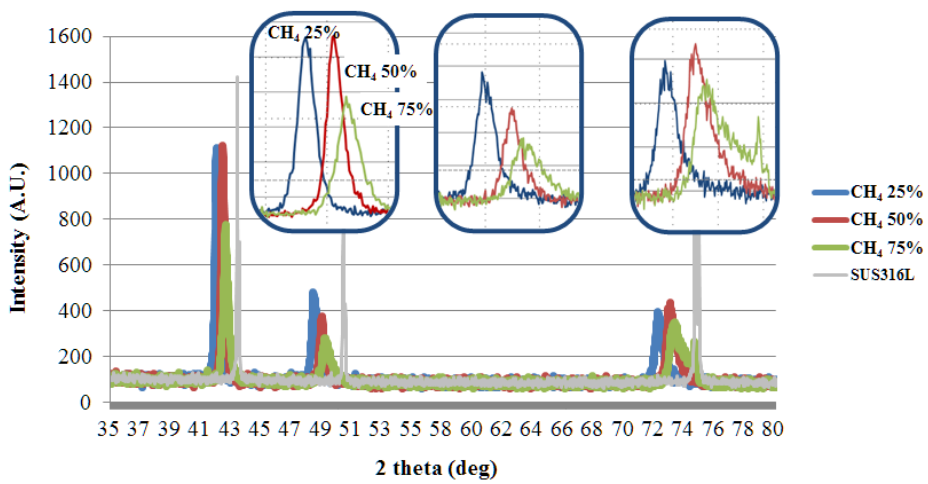

Figure.4-8 x-ray diffraction patterns of carburized AISI 316L with X_{CH4} (25,50,75%)

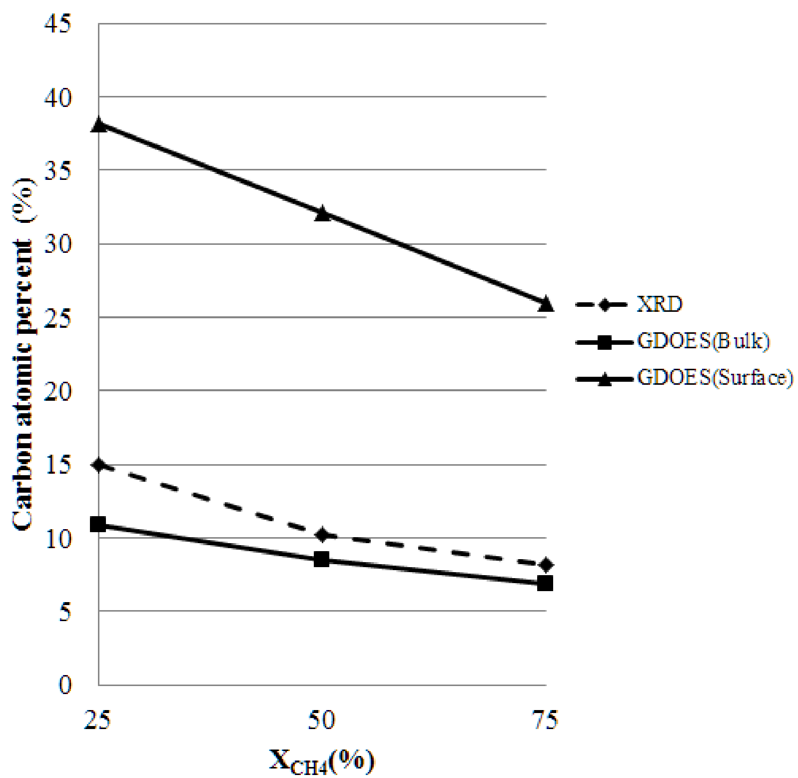

Figure.4−9 Carbon atomic percent analyzed by GD−OES and XRD

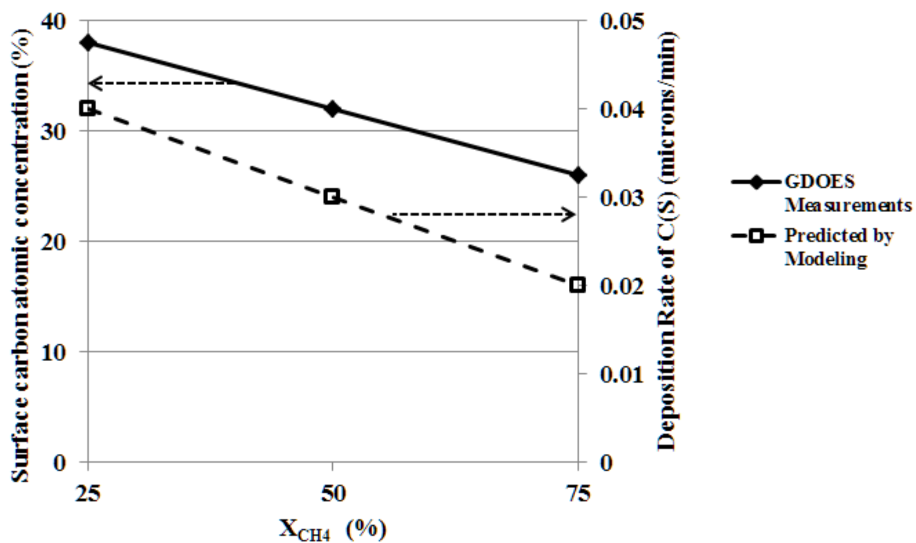

Figure.4-10 Comparison of deposition rates of C(s) predicted by plasma modeling and surface carbon atomic concentration measured by GDOES as a function of X_{CH4} fraction

V. Conclusion

In this study, a plasma model was constructed to understand the plasma carburizing process and the predictions of the model was compared with test results. When the methane fraction was increased and the Ar fraction was decreased, both model and test results showed decreasing trends in N_e and T_e. As the methane fraction was decreased in the plasma volume, the density of CH_x and the supply of carbon to the surface of the substrate were increased, which accelerated the formation of carbon layer on the surface. XRD and GDOES confirmed that the carbon concentration in the sample surface and inside of substrate decreased at high methane fractions. Test result showed a proportional relationship between the carbon concentrations of surface and inside of substrate. By applying this relationship in the plasma model, the carbon concentration in the inside of substrate was predicted with the calculated free carbon concentration on the surface. Based on the test results, the deposition rate of C(s) was predicted using the plasma carburizing numerical model and the predictions showed matching values to the experimental results.

VI. Reference

[1] W. Hong:Journal of The Korean Institute of Surface Engineering 46 (2013)192.

[2] K. Tokaji, K. Kohyama, M. Akita, International Journal of Fatigue 26 (2004)543.

[3] K. Fenga, T. Hub, X. Zhuguo Li, P.K. Chu, Journal of Power Sources 199 (2012) 207.

[4] S. Adachi, N. Ueda, Advanced Powder Technology 24 (2013)818.

[5] W. Li, X. Li, H. Dong, Acta Materialia 59 (2011)5765.

[6] Y. Sun, Materials and Design 30 (2009)1377.

[7] Y. Sun, Surface & Coatings Technology 228 (2013)342.

[8] C.J. Scheuer, R.P. Cardoso, M. Mafra, S.F. Brunatto, Surface & Coatings Technology 214 (2013)30.

[9] A.M.F. Trindade, J. Escada, P.N.B. Neves, T.H.V.T. Dias, J.A.S. Barata, F.P. Santos and C.A.N. Conde: JINST 7 (2012) P06010

[10] M. A. Lieberman and A. J. Lichtenberg:Principles of Plasma Discharges and Materials Processing(Wiley, New York, 2005) 2nd ed.

[11] I.B Denysenko, S.Xu, J.D. Long, P.P.Rutkevych,

N.A.Azarenkov, K.Ostrikov: Journal of Applied Physics 95(2004)5

[12] A. von Keudell, M. Meier, and C. Hopf:Diamond Relat. Mater.11(2002)969.

[13] S. Petera, K. Graupner, D. Grambole, and F. Richte:J. Appl. Phys.102(2007) 053304.

[14] F. J. Gordillo–Va and J. M. Albella:J. Appl. Phys.94(2003) 6085.

[15] K. Teii and T. Yoshida:J. Appl. Phys.85(1999) 1864.

[16] Y. B. Guo and F. C. N. Hong:Diamond Relat. Mater.12(2003) 946.

[17] J. Zhou, I. T. Martin, R. Ayers, E. Adams, D. Liu, and E. R. Fisher:Plasma Sources Sci. Technol.15(2006) 714.

[18] K. Teii, M. Hori, and T. Goto:J. Appl. Phys.92(2002) 4103.

[19] K. Okada and S. Komatsu:J. Vac. Sci. Technol. A20(2002) 1835.

[20] K. Okada, S. Komatsu, and S. Matsumoto:J. Vac. Sci. Technol. A21(2003) 1988.

[21] D. Herrebout, A. Bogaerts, M. Yan, R. Gijbels, W. Goedheer, and D. Dekempeneer:J. Appl. Phys.90(2001) 570.

[22] S. F. Yoon, K. H. Tan, Rusli, and J. Ahn:J. Appl. Phys.91(2002) 40.

[23] S. F. Yoon, K. H. Tan, Rusli, and J. Ahn:J. Appl. Phys.91(2002) 1634.

[24] I. B. Denysenko, S. Xu, J. D. Long, P. P. Rutkevych, and N. A. Azarenkov:J. Appl. Phys.95(2004) 2713.

[25] K. Tachibana, M. Nishida, H. Harima, and Y. Urano:J. Phys. D17(1984)1727.

[26] M. A. Lieberman and R. A. Gottscho: inPhysics of Thin Films, ed. M. Francombe and J. Vossen (Academic, New York, 1994) Vol. 18, p. 1.

[27] C. Lee, D. B. Graves, M. A. Lieberman, and D. W. Hess:J. Electrochem.Soc.141(1994) 1546.

[28] C. Lee and M. A. Lieberman:J. Vac. Sci. Technol. A13(1995) 368.

[29] A. von Keudell and W. Moller:J. Appl. Phys.75(1994) 7718.

[30] N. V. Mantzaris, E. Gogolides, A. G. Boudouvis, A. Rhallabi, and G.

Turban:J. Appl. Phys.79(1996) 3718.

[31] E. Gogolides, D. Mary, A. Rhallabi, and G. Turban:Jpn. J. Appl. Phys.34(1995) 261.

[32] K. Bera, B. Farouk, and Y. H. Lee:Plasma Sources Sci. Technol.10(2001)211.

[33] M. J. Druyvesteyn:Z. Phys.64(1930) 781[in German].

[34] T. Kimura and K. Ohe:Rev. Sci. Instrum.64(1993) 3274.

[35] T. Kimura and H. Kasugai:J. Appl. Phys.107(2010) 083308.

[36] R. K. Janev, W. D. Langer, K. Evans, Jr., and D. E. Post, Jr.:Elementary Processes in Hydrogen–Helium Plasmas(Springer, New York, 1987).

[37] H. Tawara: inAtomic and Molecular Processes in Fusion Edge Plasmas,ed. R. K. Janev (Plenum, New York, 1995) p. 461.

[38] D. A. Alman, D. N. Ruzic, and J. N. Brooks:Phys. Plasmas7(2000) 1421.

[39] C. Hopf, T. Schwarz−Selinger, W. Jacob, and A. von Keudell:J. Appl.Phys.87(2000) 2719.

[40] V. A. Godyak:Soviet Radio Frequency Discharge Research(Delphic Associates, Falls Church, VA, 1986).

[41] R. Zorat, J. Goss, D. Boilson, and D. Vender:Plasma Sources Sci. Technol.9(2000) 161.

[42] L. A. Viehland and E. A. Mason:At. Data Nucl. Data Tables60(1995) 37.

[43] H. W. Ellis, R. Y. Pai, E. W. McDaniel, E. A. Mason, and L. A. Viehland:At. Data Nucl. Data Tables17(1976) 177.

국문초록

최근에는 연료전지에 사용하는 금속재질의 2극 극판의 성능을 향상시키기 위해 메탄과 알곤을 사용한 플라즈마 침탄처리 공정에 대한 연구가 활발히 진행되고 있다. 일반적으로 플라즈마를 사용하지 않은 열에너지를 활용하여 금속재질의 모재에 침탄처리를 하면 경도는 향상되지만 내부식성은 악화된다. 하지만 유도결합 플라즈마를 활용하면 낮은 온도에서 침탄을 진행할 수 있으며 이는 크롬의 Depletion을 방지할 수 있어 우수한 내부식성을 갖게 된다. 본 연구에서는 유도결합 플라즈마를 활용하여 기판에 도달하는 이온과 라디칼의 농도는 높게 유지하면서도 저온공정을 가능하게 하였다.

플라즈마 침탄공정의 주요 인자는 ICP Power, 공정압력, 공정 Gas, 기판Bias 등이다. ICP power, 공정압력을 조절하면 기판으로 입사하는 이온, 라디칼의 종류, Flux를 조절가능하고, Bias를 조절하면 ion의 energy를 조절하면서 Carburizing 실험을 하면 경향성 있는 공정결과를 확인할 수 있다. 따라서 메탄 플라즈마에 존재하는 이온의 종류 및 밀도에 대한 연구가 필수인 것을 알 수 있다. 이온의 density를 측정은 일반적으로 Langmuir probe, Quadrupole mass spectrometer(QMS), Optical emission spectroscopy(OES), laser induce fluorescence (LIF)등을 사용한다. Langmuir probe의 경우 플라즈마에 존재하는 라디칼이나 이온종류에 대한 측정이 불가능하기 때문에 본 연구에 활용하기에는 부족한 점이 많다. 게다가 측정하는 범위가 Langmuir probe의 실제표면적이 아닌 probe 부근에 형성된 Sheath와 맞닿아 있는 플라즈마 표면적에 대한 정보임

을 감안해야 하기 때문에 Langmuir probe의 경우 해당 공정의 Sheath size에 대한 해석이 추가로 필요하다. 하지만 sheath size에 대한 해석결과도 오차를 포함하고 있으므로 세밀한 주의가 필요한 분석법이다. 또한 플라즈마 내부로 삽입된 probe에 의해 이차전자 방출, 탐침표면의 화학종들이 흡착되기 때문에 반응성이 높은 gas 사용시의 제한이 되는 등의 단점이 있다. OES는 전자나 이온에 의해 여기 된 species들이 다시 바닥상태로 전이될 때 발생하는 wave에 대한 정보를 기준으로 측정을 하게 되는데 여기가 잘되지 않은 질량이 큰 화학종에 대한 정보는 알기가 어렵고 정량적인 해석을 위해서는 종종 Ar actinometry를 사용하여 특정 파장의 세기와 Ar에 의한 파장의 세기를 고려 해야 하고 검출되는 피크들에 대한 명확한 해석이 어려운 단점이 있다. 또한 공정이 진행되는 기판 부근에 대한 정보를 얻기가 불가능한 단점이 있다. QMS는 필라멘트를 가열하여 튀어나온 열 전자를 사용하여 중성종을 이온으로 만들고 사중극자로 구성된 질량 필터를 이온이 통과하면서 중성입자 및 이온의 질량을 측정하는 방법이다. 따라서 유체모델을 기반으로 한 methane plasma chemistry에 대한 계산을 통해 기판위치에서의 화학종에 대한 정보를 얻을 수 있다.

본 연구에서는 상용프로그램인 CFD-ACE+를 사용하여 메탄 플라즈마 모델링과 침탄공정 모델링을 진행하였다. 침탄공정 모델링은 실험결과를 잘 설명하는 것이 목적이기 때문에 실제 침탄실험을 진행 한 뒤 비교하였다. 실험조건으로는 알곤과 메탄가스의 비율을 조절하면서 진행하였고, 그 비율에 따라 경향성 있는 침탄 결과를 확인할 수 있었다. 알곤의 비율을 높이고 메탄가스의 비율을 3:1까지 줄여줄수록 실험재료인 AISI316L내에 존재하는 탄소 농도가 증가

하는 것을 확인 할 수 있었다. 실험조건에서 가스 비율을 제외한 다른 조건들은 동일하게 진행했기 때문에 입사하는 이온의 에너지는 큰 차이가 없을 것이며 입사하는 라디칼이나 이온의 종류와 양의 변화가 있을 것이다.

실험조건과 동일하게 알곤과 메탄의 비율을 변화시키며 플라즈마 모델링을 수행한 결과 플라즈마에 존재하는 Hydro-Carbon 종들의 비율 변화를 확인 할 수 있었다. 알곤을 많이 넣어줄수록 $C_2H_x^+$ 보다는 CH_x^+이 많이 형성되는 것을 확인 할 수 있었고, 이는 메탄이 분해반응을 하면서 에너지를 소모하기 때문에 메탄비율이 작아질수록 증가하는 전자온도와도 연관하여 설명이 가능하다. 메탄을 활용한 diamond like carbon막의 증착공정과 달리 침탄공정은 기판 위에 증착된 막의 두께에 대한 영향보다는 막내에 존재하는 탄소의 농도에 영향을 받는다. 이는 침탄공정이 확산공정임을 다시 한번 확인해 준다. 막에 존재하는 탄소의 정량을 분석하기 위해 GD-OES 분석을 실시하였고 AISI316L내부에 존재하는 탄소의 농도를 분석하기 위해 GD-OES와 XRD분석을 활용하였다. 침탄공정이 확산공정이기 때문에 플라즈마 모델링을 활용하여 기판에 쌓이는 막에 존재하는 탄소의 농도를 계산 가능하며 이는 실험에서 확인한 경향성과도 일치하는 결과임을 확인하였다.

주요어 : 유도결합 플라즈마, ICP, 침탄, 플라즈마 시뮬레이션, CFD-ACE, plasma chemistry

학번 : 2012-20575